Check for updates

Metal organic framework derived NiO$_x$ nanoparticles for application as a hole transport layer in perovskite solar cells

Md. Ariful Islam,[a] Vidhya Selvanathan,*[f] Puvaneswaran Chelvanathan,[a] M. Mottakin,[ab] Mohammod Aminuzzaman,[c] Mohd Adib Ibrahim, [iD][a] Ghulam Muhammad [iD][d] and Md. Akhtaruzzaman [iD] *[ae]

NiO$_x$ as a hole transport layer (HTL) has gained a lot of research interest in perovskite solar cells (PSCs), owing to its high optical transmittance, high power conversion efficiency, wide band-gap and ease of fabrication. In this work, four different nickel based-metal organic frameworks (MOFs) using 1,3,5-benzenetricarboxylic acid (**BTC**), terephthalic acid (**TPA**), 2-aminoterephthalic acid (**ATPA**), and 2,5-dihydroxyterephthalic acid (**DHTPA**) ligands respectively, have been employed as precursors to synthesize NiO$_x$ NPs. The employment of different ligands was found to result in NiO$_x$ NPs with different structural, optical and morphological properties. The impact of calcination temperatures of the MOFs was also studied and according to field emission scanning electron microscopy (FESEM), all MOF-derived NiO$_x$ NPs exhibited lower particle size at lower calcination temperature. Upon optimization, Ni-TPA MOF derived NiO$_x$ NPs calcined at 600 °C were identified to be the best for hole transport layer application. To explore the photovoltaic performance, these NiO$_x$ NPs have been fabricated as a thin film and its structural, optical and electrical characteristics were analyzed. According to the findings, the band energy gap (E_g) of the fabricated thin film has been found to be 3.25 eV and the carrier concentration, hole mobility and resistivity were also measured to be 6.8×10^{14} cm^{-3}; 4.7×10^{14} Ω cm and 2.0 cm^2 V^{-1} s^{-1}, respectively. Finally, a numerical simulation was conducted using SCAPS-1D incorporating the optical and electrical parameters from the thin film analysis. FTO/TiO$_2$/CsPbBr$_3$/NiO$_x$/C has been utilized as the device configuration which recorded an efficiency of 13.9% with V_{oc} of 1.89 V, J_{sc} of 11.07 mA cm^{-2}, and FF of 66.6%.

1 Introduction

Metal oxide nanostructures possess numerous unique features that become distinct from those present in the bulk solid state due to their size differences. Particle size reduction in the nanoscale domain offers a variety of unique characteristics, including low sintering temperature, large specific surface area and quantum size effect.[1] Out of all the metal oxides, NiO$_x$ nano-structures have received substantial scientific interest owing to their high band gaps (3.6–4.0 eV) and p-type electrical conductivity characteristics.[2] Moreover, NiO$_x$ nanoparticles (NPs) offer a number of applications including in battery cathodes,[3] as catalysis,[4] electrodes of fuel cells, in the field of electrochromic films,[5] gas sensors[6] and magnetic materials.[7] Additionally, NiO$_x$ NPs are also being used in smart windows,[8] as the effective hole transporting layer (HTL) in PSCs,[9] dye-sensitized photocathodes[10] and electrochemical super-capacitors.[11] As a hole transport layer (HTL), NiO$_x$ is very promising for PSCs because of its deep valence band, affordable cost, high optical transmittance and outstanding stability.[12,13] Recently, a number of experiments have been conducted on NiO$_x$-based PSCs to make the device more reliable and efficient. In order to generate a uniform and homogenous thin film, Pei-Huan Lee *et al.* conducted an emulsion process to synthesize NiO$_x$ NPs. Using this thin film, they achieved a PCE of 18%.[13] Shuangjie Wang *et al.* applied an ionic liquid (NiO$_x$-IL) during the synthesis process and they found a promising PCE of 22.62%.[14] The structural, electrical, optical, compositional and magnetic properties of NiO$_x$ NPs are highly dependent on the

[a]*Solar Energy Research Institute (SERI), Universiti Kebangsaan Malaysia (UKM), 43600 Bangi, Selangor, Malaysia. E-mail: akhtar@ukm.edu.my*

[b]*Department of Applied Chemistry and Chemical Engineering, Bangabandhu Sheikh Mujibur Rahman Science and Technology University, Gopalganj-8100, Bangladesh*

[c]*Department of Chemical Science, Faculty of Science, Universiti Tunku Abdul Rahman (UTAR), Perak Campus, Jalan Universiti, Bandar Barat, 31900 Kampar, Perak D. R., Malaysia*

[d]*Department of Computer Engineering, College of Computer and Information Sciences, King Saud University, Riyadh, Saudi Arabia*

[e]*Graduate School of Pure and Applied Sciences, University of Tsukuba, Tsukuba, Ibaraki 305-8573, Japan*

[f]*Institute of Sustainable Energy, Universiti Tenaga Nasional (The Energy University), Jalan Ikram-Uniten, Kajang 43000, Selangor, Malaysia*

synthesis process, particle size and shape. Generally, the experimental route adopted for the synthesis of NiO_x NPs is very crucial in governing a number of key factors, including crystallinity, size and shape, composition-purity of the final product.[15] So far, in comparison to other conventional methods like spray-pyrolysis, co-precipitation, sol–gel, microwave pyrolysis, thermal decomposition; solvothermal is an efficient and simple technique for the synthesis of NPs because it offers comparatively large specific surface area with low temperature processing step.[16] Solvothermal technique has successfully overcome challenges such as utilization of expensive specialized equipment, low energy usage, high purity and large-scale manufacturing.[16] Considering all of these, much effort has been devoted in recent past to the development of metal–organic frameworks (MOFs) as precursors utilized in the synthesis process of porous oxides. Basically, MOFs are defined as porous hybrid compound, that consist of metal ions which are connected with organic ligands *via* coordination bond and create a three-dimensional framework.[17,18] In comparison, MOFs offer a wider range of options to design and construct the hierarchically nanostructures, a class of polyfunctional compounds with a number of morphological and topological characteristics.[19]

Most studies have stated that the morphology and size of particles of the metal oxides derived from MOF depends on the chemical structure of the ligand used which in turn, tunes the overall architecture. Typically for any NP synthesis, the homogeneity, NPs shape and size can be tuned by changing the solution concentration, pH, nucleation rate, reaction temperature and presence of complexing agent in the synthesis process.[20] Among these factors, calcination temperature is very important because it alters the shape and morphological properties of nanoparticles as well as creating defects, which leads to the formation of new energy state.[21] The phase of the materials is often influenced by the sintering temperature, which in turn affects the materials' structural and optical properties.[21] So, its highly necessary to calcine the produced nanoparticles at elevated temperatures in order to obtain single phase nanostructures of the right size.[20] The removal of impure phases, and an improvement in particle density and a rise in crystallites are some potential benefits of this step.[20] For synthesis of MOF derived NPs, it is essential to ensure the calcination temperature is high enough to produce high purity metal oxides while at the same time ensure particles with desired size and shape is produced.

This article addressed the synthesis process of NiO_x NPs derived from metal–organic framework by utilizing four distinct ligands namely 1,3,5-benzenetricarboxylic acid (**BTC**), terephthalic acid (**TPA**), 2-aminoterephthalic acid (**ATPA**), 2,5-dihydroxyterephthalic acid (**DHTPA**). The effect of different ligand structure of the MOF precursors calcined at different temperature on the structural, morphological and optical properties of the synthesized NiO_x NPs was analyzed. In extension the MOF derived NPs were applied as potential hole transport layer (HTL) in n-i-p PSCs to elucidate the future potential as component in energy storage devices.

2 Materials and methods

2.1 Materials

All chemicals and reagents were utilized, without additional purification. $Ni(NO_3)_2 \cdot 6H_2O$; 1,3,5-benzenetricarboxylic acid (**BTC**), terephthalic acid (**TPA**), 2-aminoterephthalic acid (**ATPA**), 2,5-dihydroxyterephthalic acid (**DHTPA**), dimethylformamide (DMF), ethanol, KOH, methanol, acetone, absolute ethanol (99.9%), acetic acid, ethylene glycol, 1-ethyl-3-methylimidazolium tetrafluoroborate, fluorine doped tin oxide (FTO) coated soda-lime glass substrate (SLG), were pursed from Sigma Aldrich, Germany.

2.2 Synthesis of MOF derived NiO_x NPs

The MOF-derived NiO_x NPs were synthesized by solvothermal method (Fig. 1). For this experiment, 2.1 mmol $Ni(NO_3)_2 \cdot 6H_2O$ and 3 mmol ligand (**BTC/TPA/ATPA/DHTPA**) were well dispersed in 15 mL dimethylformamide (DMF). The resulting dispersed solutions were placed in 100 mL Teflon-polytetrafluoroethylene coated autoclave with stainless steel jacket at 160 °C for 12 h. After completing the reaction, the colloidal solutions were taken out from autoclave and left it for cooling down to ambient temperature naturally. After centrifuging the colloidal solution, it was repeatedly rinsed with ethanol and water for 3 times. Then the colloidal solutions were centrifuged and rinsed with ethanol and water for several time. The products were dried in an oven at 80 °C for 8 h to obtain MOFs. Finally, these Ni-MOFs were calcined in a furnace for 5 hours at different temperature (600 °C, 700 °C, and 900 °C) to achieve the desired NiO_x nanoparticles.

2.3 Fabrication of NiO_x thin film

Bare SLG and FTO coated SLG were used as a substrate for the deposition of NiO_x thin films. Bare SLG has been utilized to measure the thin film's electrical characteristics, while FTO coated SLG was used to evaluate the film's structural and optical characteristics. The substrates were cleaned by using an ultrasonic cleaner with ethanol, acetone, and DI water; afterwards dried with a stream of N_2 gas. Prior to spin coating, all substrates were treated for 15 min with UV-ozone plasma. NiO_x colloidal dispersion was prepared by dissolving 40 mg NiO_x synthesized powder into 2 mL absolute ethanol with the concentration of 20 mg mL^{-1} 30 μL acetic acid, 150 μL ethylene glycol and 500 μL ionic liquid (BMIMBF$_4$) have also been incorporated to make a homogenous dispersion. The dispersion was subsequently coated onto the glass substrate with the speed of 4000 rpm for 30 s, followed by 10 min of baking at 200 °C on a hot plate. Finally, the films calcined at 300 °C for 1 h into a furnace. All of these operations were performed under ambient conditions.

2.4 Nanoparticles and thin film characterization

The morphological and structural characteristics of MOF-derived NiO_x NPs and thin film were carried out by using several characterization approaches such as X-ray diffraction
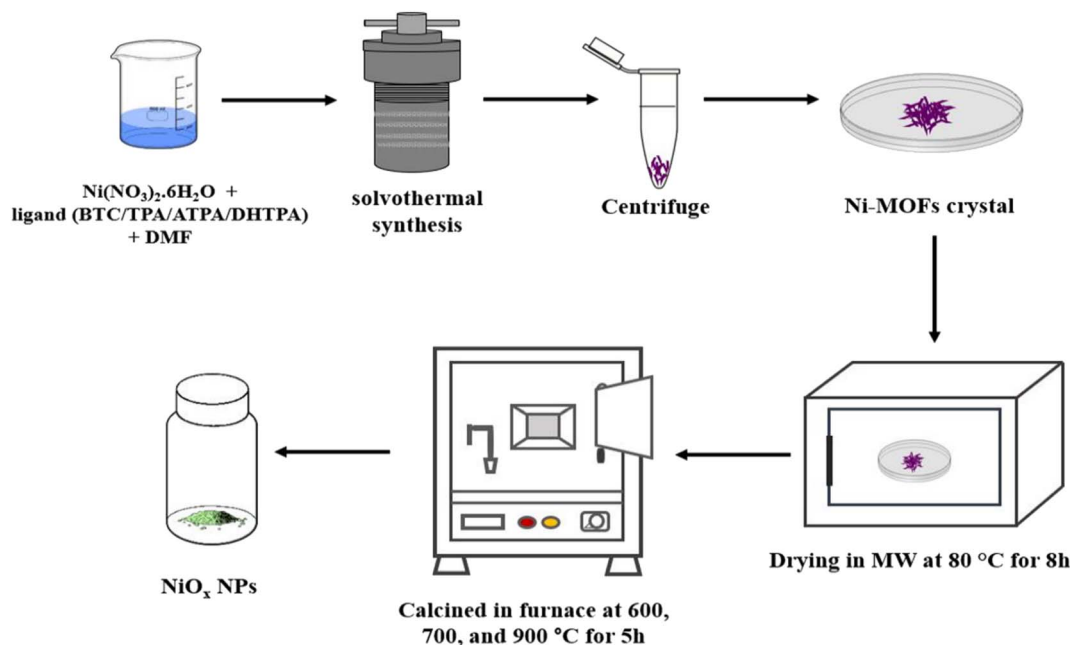
Fig. 1 Synthesis process of MOF-derived NiO$_x$ NPs.

(XRD), field emission scanning electron microscope (FeSEM), absorption spectra (UV-Vis) coupled with Fourier transform infrared (FTIR). The XRD were measured in the 2θ with a region of 10° to 90° for NPs and 10° to 80° for thin film respectively utilizing an X-ray diffractometer 'BRUKER aXS-D8 Advance Cu-Ka'. For the detection of functional group, Bruker FTIR spectrometer has been used with spectral range from 4000 to 500 cm^{-1}. To investigate the grain size, surface morphology and growth of NPs FeSEM model 'LEO 1450 VP' was utilized. UV-Vis spectrophotometer PerkinElmer Lambda 35 was being used to evaluate optoelectronic characteristics, including optical absorbance and transmittance. The electrical characteristics of thin film were measured, using the HMS ECOPIA 3000 Hall effect measuring system under a magnetic field (0.57 T).

3 Results and discussion

3.1 Properties of MOF derived NiO$_x$ nanoparticle

3.1.1 Structural properties. Fig. 2 depicts the XRD pattern of NiO$_x$ NPs obtained from MOFs employing four different ligand following calcination at 600 °C, 700 °C, and 900 °C. It has been revealed that, all of the NiO$_x$ NPs sample showed five major diffraction intensity at 2θ with the values of 37.2°, 43.2°, 62.8°, 75.4°, and 79.4°, were exactly indexed as the cubic structure's crystallographic plane of (111), (200), (220), (311), and (222) [JCPDS, No. 04-0835], which is in excellent agreement with previous diffractogram values of NiO$_x$.[22,23] A noticeable peak intensities variation was also evident among the sample, when sintered at 600 °C and 700 °C and 900 °C. The degree of crystallinity of NPs reduced at lower calcination temperature because, at lower heat treatment certain carbon residues still remain in the synthesized powder.

Highly pure NiO$_x$ can be obtained with high sintering temperature (900 °C), result in sharp peak intensity. NiO$_x$-BTC (700 °C); NiO$_x$-ATPA (600 °C and 700 °C); and NiO$_x$-DHTPA (600 °C), all exhibit two faint peaks at 2θ with the value of around
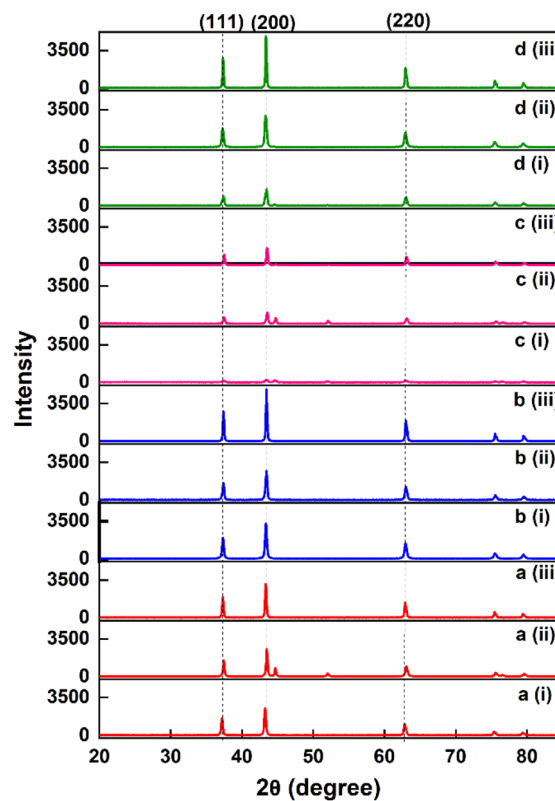

Fig. 2 X-ray diffractogram of MOF-derived NiO$_x$ nanoparticles (a) NiO$_x$-BTC (b) NiO$_x$-TPA (c) NiO$_x$-ATPA and (d) NiO$_x$-DHTPA mediated calcined at (i) 600 °C and (ii) 700 °C (iii) 900 °C.

Table 1 Average crystallite size and strain of NiO_x NPs with different calcination temperature

Material	Calcination temperature (°C)	Average crystallite size (nm)	Average strain (ε)
NiO_x-BTC	600	24.77	0.0029
	700	25.69	0.0029
	900	29.54	0.0025
NiO_x-TPA	600	23.79	0.0030
	700	24.34	0.0030
	900	30.81	0.0023
NiO_x-ATPA	600	20.60	0.0037
	700	22.20	0.0027
	900	28.03	0.0026
NiO_x-DHTPA	600	21.90	0.0033
	700	22.27	0.0033
	900	31.39	0.0023

44.8° and 51.7° due to impurities in the synthesized powder. With the help of Scherer's formula, the average crystal sizes (D) were determined:[24]

$$D = \frac{0.94\lambda}{\beta \cos \theta} \quad (1)$$

where, D is the average (Avg) crystallite size; β is the FWHM width of the diffraction peak; λ is the wavelength X-ray; and θ is the diffraction angle.

Table 1 shows that crystallite size increases along with a rise in sintering temperature. At higher heat treatment, particles imperfections, edges and flaws are removed, resulting in large size crystallites with definite crystalline phase.[25]

Furthermore, peak stretching or broadening is relayed to the quantum confinement and lattice strain effect of NPs because of its large crystallite size and grain boundaries, respectively. To investigate the influence of strain on the structural characteristics of NiO_x nanoparticles, Williamson Hall (W–H) analysis is introduced. The W–H equation is represented as[26]

$$\beta \cos \theta = \frac{K\lambda}{D} + 4\varepsilon \sin \theta \quad (2)$$

where, β is the FWHM width of the diffraction peak obtained at particular angle θ, D is the average crystallite size; θ is the diffraction angle; K is the shape factor with the value of 0.9; λ is the wavelength of the X-ray and ε is crystallite strain.

Table 1 further demonstrates the relation between strain and crystallite size of NiO_x NPs. It has been observed that the strain reduces as the size of the crystallites increase. The reason for this behavior is the possibility of impurities and defects in NPs and also the surface area is vast in contrast.[26] Therefore, XRD indicates that NiO_x-TPA (900 °C) and NiO_x-DHTPA (900 °C) has the least strain value approximately 0.0023, compared to other NPs, indicating that they are highly crystalline with less structural flaws.

Fig. 3 illustrates the FTIR absorption spectra of all synthesized Ni-MOFs and their corresponding NPs. FTIR study of Ni-BTC MOF has been described in Fig. 3a. The formation of Ni-BTC MOFs has been confirmed by obtaining a significant shift in the carbonyl (–CO–) groups at 1608 cm^{-1}, suggesting that the ligand's carboxylate moieties have been deprotonated and coordinated with Ni^{2+}. Moreover, the Ni–O stretching vibration is characterized by a strong absorption spectrum at 724 cm^{-1}. O–H stretching was found as a wideband at 2800–3500 cm^{-1}, suggesting the coordinated water molecule in Ni-BTC MOF prior to activation.[27] Fig. 3b depicts the FT-IR spectra of the Ni-TPA metal–organic framework. As shown in Fig. 3b, Ni-TPA MOF exhibits two prominent peaks at around 1380 cm^{-1} and 1580 cm^{-1} accordingly, which are due to the symmetric and asymmetric stretching of ligand's carboxyl (–COO$^-$) group. Separating the stretching modes indicated that TPA ligand's –COOH groups were linked to Ni^{2+} ions through a bidentate binding manner.[28] Narrow and weak bands at 1025 cm^{-1} is owing to the stretching (C–H) and bending (C–H) of aromatic ring, which indicating the presence of organic ligand in the MOF. The wide peaks in between 3400–3600 cm^{-1} may be attributed owing to acidic –OH or crystal water.[29] Investigation of the FTIR spectra of Ni-ATPA MOF as shown in Fig. 3c, indicating –NH$_2$ stretching vibration at around 3308 cm^{-1}. The absorption peaks at around 1387–1689 cm^{-1} may be detected owing to symmetric and asymmetric stretching vibrations of the –COOH groups. Moreover, O–Ni–O vibrational peaks had been found at 530 cm^{-1} and 668 cm^{-1} in respective Ni-ATPA MOF, indicating the establishment of the coordination bonding among the –COOH groups from ATPA and Ni^{2+}.[30] For the Ni-DHTPA, the benzene rings out-of-plane vibrational peak detected at around 888 cm^{-1} (Fig. 3d). For carboxylate groups, symmetric and asymmetric stretching appears at around 1410 cm^{-1} and 1556 cm^{-1}. The interlayer water and C–O–H contribute to the wide band at 3425 cm^{-1}. This implies that Ni^{2+} has been effectively coordinated with DHTPA ligand.[31,32]

In respect of FTIR spectra study, all NiO_x-MOF derived NPs showed the absorption in similar region and there were no traces of peaks attributed to ligands in the MOF. This observation verifies that the Ni-MOF structures were completely transformed into NiO_x upon calcination even at 600 °C. It has been observed that, O–Ni–O vibrations are responsible for the FTIR spectrum peak about 663 and 443 cm^{-1}. Furthermore, the wide peak at 1398, 3422 and 1622 cm^{-1} can be ascribed to stretching and bending vibration of the hydroxyl group captured on the surface of the catalyst from the environment
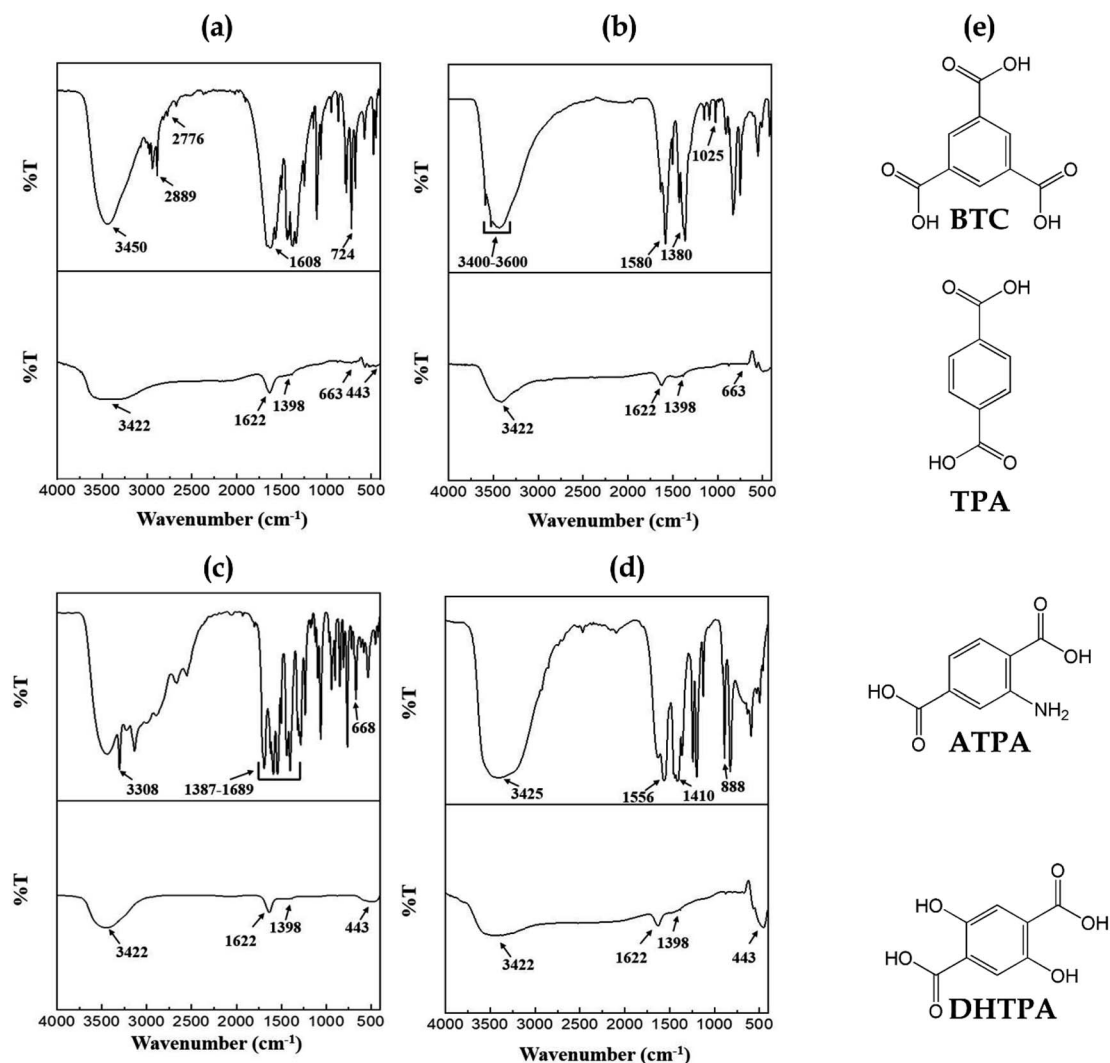
Fig. 3 FTIR spectral absorption of synthesized Ni-MOFs and its corresponding NiO_x NPs (a) Ni-BTC (b) Ni-TPA (c) Ni-ATPA (d) Ni-DHTPA and (e) the chemical structures of ligands.

during FTIR examination. The symmetric and asymmetric stretching of C–O and O–C=O may also be appeared with a narrow band intensity with the range between 1000–1500 cm^{-1} that indicating a strong physical absorption to CO_2 and H_2O.[23,33]

3.1.2 Morphological properties. To investigate the morphological characteristics of synthesized MOFs and their corresponding NiO_x nanoparticles, FeSEM images have been taken and the impacts of different sintering temperature on NPs morphology has also been thoroughly investigated. Fig. 4 shows the morphological properties of Ni-BTC MOF and its relevant NPs, calcined at 600 °C, 700 °C and 900 °C. It has been found that Ni-BTC MOF has a flat plate-like laminated structure that seems to be randomly arranged with high porosity (Fig. 4a). When Ni-BTC MOF was treated at 600 °C, 700 °C, and 900 °C, a systematic assessment of the morphological structure of the NiO_x NPs has been observed. NiO_x NPs seem to be well aggregated with small crystallite at calcination temperature of 600 °C (Fig. 4b); however, at 700 °C, a non-spherical random shape has

been found with less agglomeration (Fig. 4c). The particles are found to be clear, distinct crystal with spherical shapes at 900 °C (Fig. 4d). It is evident that the avg. size of particle is increased as the calcination temperature rise, which is consistent with Siamak Pilban Jahromi *et al.* study, they found that larger NiO_x NPs were obtained at higher temperature (500 °C) around 21.8 nm compare to lower calcination temperature (300 °C and 400 °C).[34]

SEM observations of the Ni-TPA MOF and relevant NPs at various sintering temperatures as illustrated in Fig. 5. Ni-TPA MOF showed hierarchical plate-like structure (Fig. 5a). NPs seem to be more compact, uniform-sized, and spherical in shape when MOF is treated at 600 °C (Fig. 5b). The well-defined nanostructures are also observed at 700 °C but the particles size is bigger than at 600 °C (Fig. 5c). For 700 °C, the nanoparticles size varied with ranging from 40 to 95 nm, whereas at 600 °C in between 25–50 nm. Particles at 900 °C have high crystallites with a spherical form, having particle sizes ranging from 85 to 130 nm (Fig. 5d).
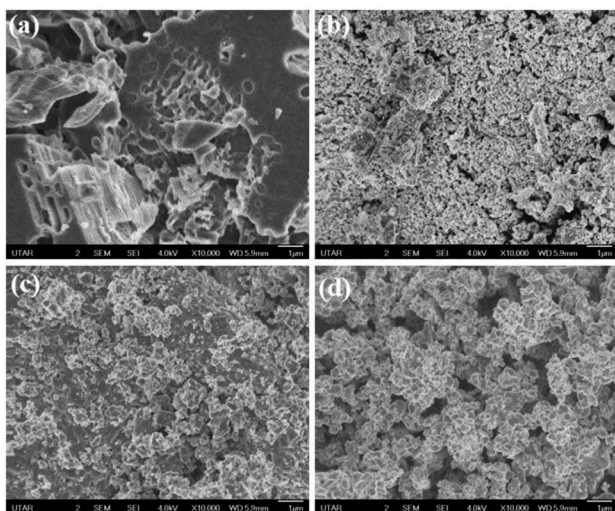
Fig. 4 FeSEM image of (a) Ni-BTC MOF and corresponding NiO$_x$ NPs calcined at (b) 600 °C (c) 700 °C (d) 900 °C.
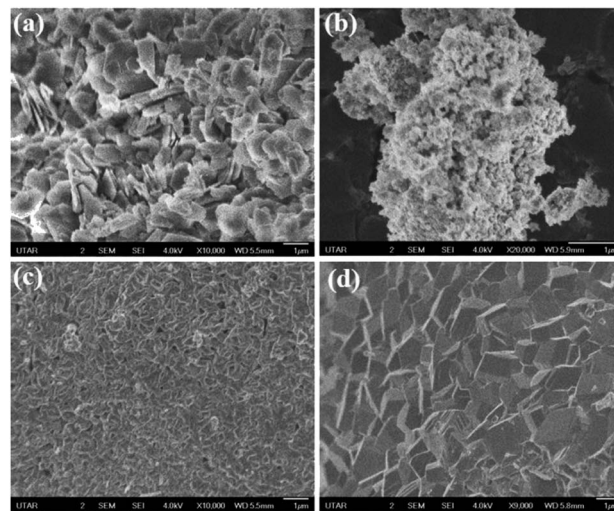

Fig. 6 FeSEM image of (a) Ni-ATPA MOF and corresponding NiO$_x$ NPs calcined at (b) 600 °C (c) 700 °C (d) 900 °C.
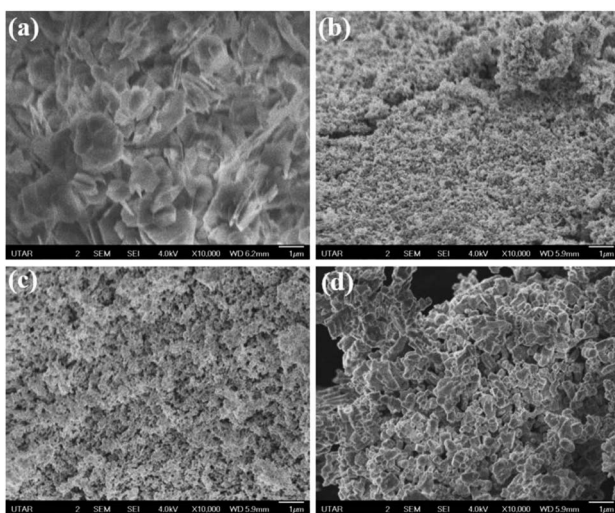

Fig. 5 FeSEM image of (a) Ni-TPA MOF and corresponding NiO$_x$ NPs calcined at (b) 600 °C (c) 700 °C (d) 900 °C.
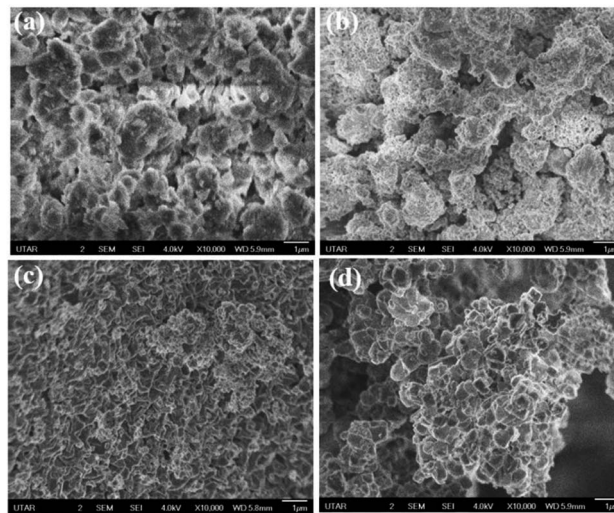

Fig. 7 FeSEM image of (a) Ni-DHTPA MOF and corresponding NiO$_x$ NPs calcined at (b) 600 °C (c) 700 °C (d) 900 °C.

With different calcination temperature, NiO$_x$ NPs derived from Ni-ATPA MOF exhibit the most morphological changes as shown in Fig. 6. For Ni-ATPA MOF hierarchical plate-like structure was obtained as like as Ni-TPA MOF (Fig. 6a). It has been observed that at 600 °C, the NPs are highly agglomerated and take on a spherical shape (Fig. 6b). The structure of the particle changes into a very compact reticular shape at 700 °C (Fig. 6c). Whereas at 900 °C, a quasi-cubic NPs structure has been identified (Fig. 6d).

The FeSEM image of Ni-DHTPA MOF also depicted a plate like structure (Fig. 7a). The NiO$_x$ nanoparticles exhibited an irregular shaped crystal structure for all sintering temperature; however, particle size and crystallinity improve with increasing temperatures (Fig. 7b–d).

3.1.3 Optical properties. Absorption spectra of NiO$_x$ NPs (calcined at 600 °C) derived from Ni-MOFs are shown in Fig. 8. For BTC-derived NiO$_x$ (NiO$_x$-BTC) NPs, a strong absorption peak has been found at around 335 nm (Fig. 8a). This absorbance is the result of an electronic transition from the valence band (V$_B$) to the conduction band (C$_B$) in NiO$_x$ NPs.[35] For TPA-derived NiO$_x$ (NiO$_x$-TPA) nanoparticles a band observed at 355 nm which is identical to previous observed value (Fig. 8b).[36] Absorption spectrum moves towards to the shorter wavelength area (hypsochromic shift) when the NPs derived from Ni-ATPA and Ni-DHTPA MOF (Fig. 8c and d). For both NiO$_x$-ATPA and NiO$_x$-DHTPA, spectral band observed at the same region around 280 nm. The movement of absorptions towards a shorter wavelength may be induced by the reduction in particle size.[37]
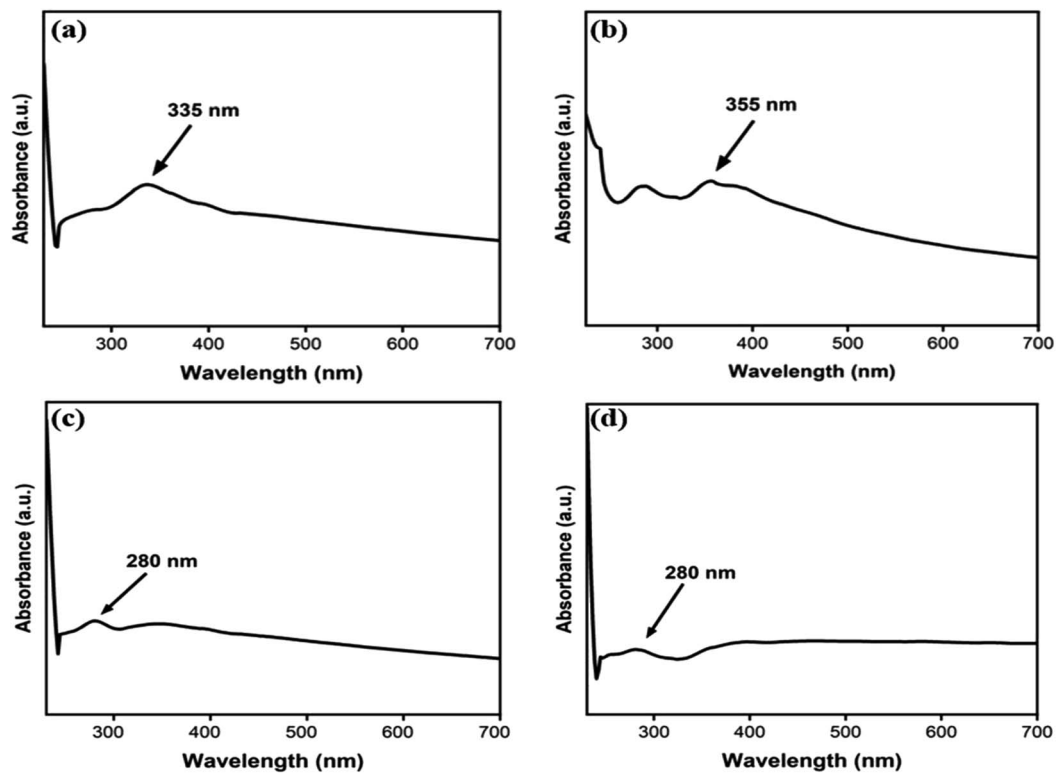
Fig. 8 UV-Visible spectra (a) NiO$_x$–BTC (b) NiO$_x$–TPA (c) NiO$_x$–ATPA (d) NiO$_x$–DHTPA nanoparticles.
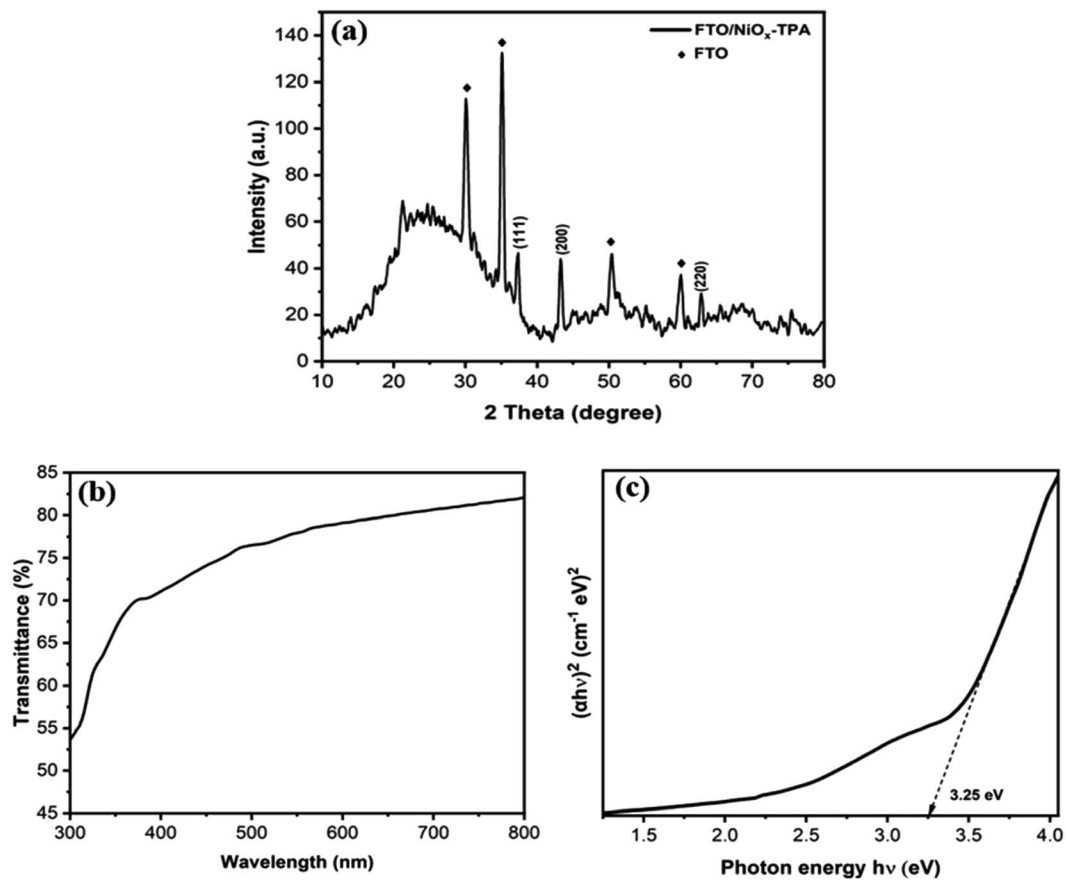

Fig. 9 Deposited NiO$_x$ thin film's (a) XRD spectrum, (b) % of transmittance (c) Tauc plot.

3.2 MOF derived NiO_x thin film as a potential hole transport layer (HTL) in perovskite solar cell

For the fabrication of NiO_x thin film as hole transport layer, it is important to ensure the material has small particle size with homogeneous distribution. Based on morphological properties discussed in previous section, TPA-derived NiO_x NPs calcined at 600 °C was selected for fabrication of NiO_x thin film. Fig. 9a depicts the XRD analysis of the NiO_x film deposited on the top of the FTO. The diffraction intensity for the NiO_x thin film have been detected at 2θ with the value of 37.0°, 43.2°, and 62.8°, which correspond to the crystallographic plane of (111), (200), and (220), respectively [JCPDS No. 73-1519]. The obtained patterns suggest a cubic phase structure, which is consistent with earlier findings.[38] The percentage of transmittance spectra for NiO_x thin film has been shown in Fig. 9b. In the visible spectrum region, the film had a high degree of transmittance with the values above 70% for the wavelength of 400 nm to

550 nm. The band gap (E_g) of the thin film was calculated using Tauc plot, as shown in Fig. 9c, and found to be approximately 3.25 eV. The following equation has been employed to calculate the value of E_g:[39]

$$(\alpha h\nu)^{\frac{1}{n}} = A(h\nu - E_g) \qquad (3)$$

where, E_g stands for the band gap; A is the constant and $h\nu$ represents the photon energy.

Furthermore, Hall measurements were conducted to determine the carrier concentration, mobility, and resistivity of the deposited thin film. Table 2 represents the findings.

To evaluate the photovoltaic performance of TPA derived NiO_x thin film, a simulation was performed by using the SCAPS-1D software with a standard spectrum of AM1.5 G (1000 W m^{-2}; $T = 300$ K) for illumination. In this simulation, synthesized NiO_x-TPA (600 °C) has been used as a hole transport layer (HTL) and TiO_2 ($E_g = 3.2$ eV) as an electron transport layer (ETL).

Table 2 Hall measurement of deposited NiO_x thin film

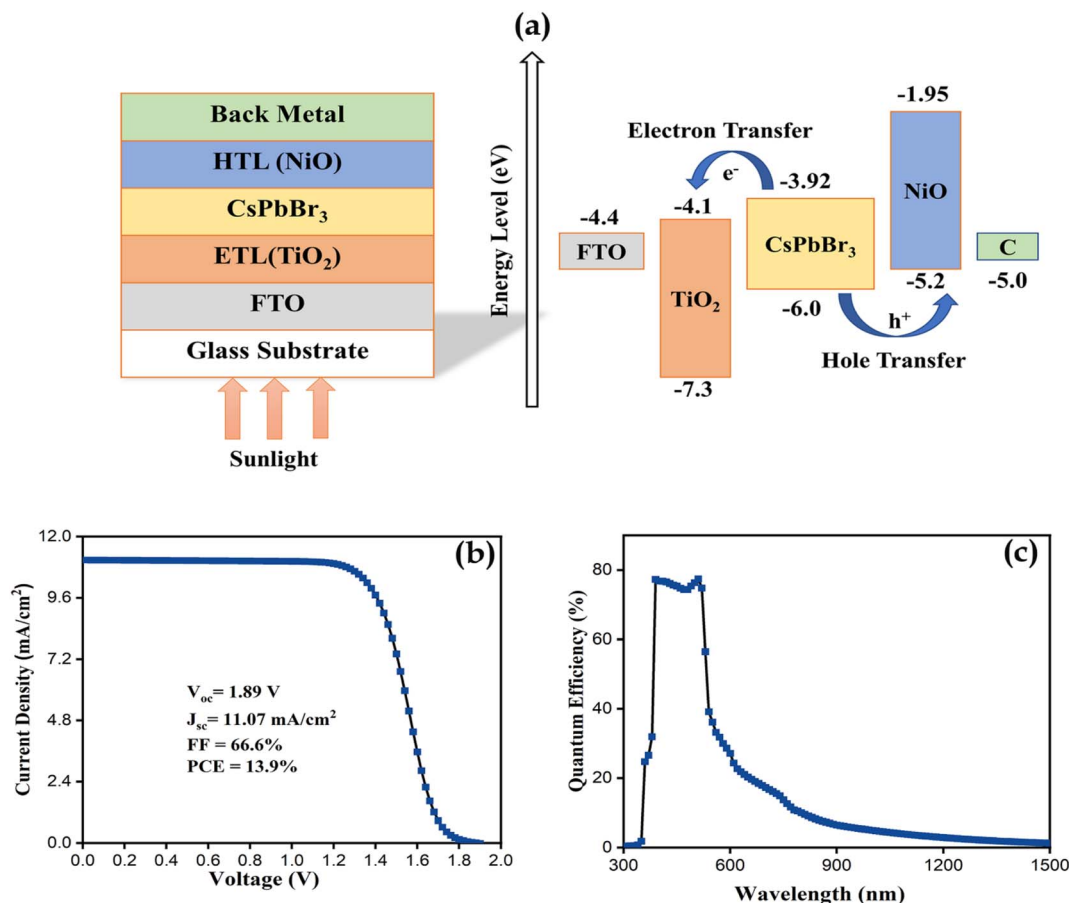| Carrier concentration (cm^{-3})	Resistivity (Ω cm)	Hole mobility (cm^2 V^{-1} s^{-1})
6.8×10^{14} (p-type)	4.69×10^3	2

Fig. 10 (a) Schematic illustration of proposed solar structure and its band energy alignment (b) J–V characteristic curves (c) quantum efficiency (Q.E) of simulated SC.

Table 3 Parameters used in device simulation

Parameters	FTO[40]	TiO₂ (ref. 40)	CsPbBr₃ (ref. 40)	NiOₓ
W (nm)	200	100	300	50
E_g (eV)	3.5	3.2	2.3	3.25 (exp.)
χ (eV)	4	4	3.6	1.8 (ref. 40)
ε_r	9	9	6.5	11.75 (ref. 40)
N_C (cm⁻³)	2.2×10^{17}	2.2×10^{18}	4.94×10^{17}	2×10^{18} (ref. 40)
N_V (cm⁻³)	2.2×10^{16}	1.8×10^{19}	8.47×10^{18}	2×10^{18} (ref. 40)
V_{th} e⁻ (cm s⁻¹)	1×10^7	1×10^7	1×10^7	1×10^7
V_{th} p (cm s⁻¹)	1×10^7	1×10^7	1×10^7	1×10^7
μ_e (cm² V⁻¹ s⁻¹)	2×10^1	2×10^1	4.5×10^3	8
μ_p (cm² V⁻¹ s⁻¹)	1×10^1	1×10^1	4.5×10^3	2 (exp.)
N_A (cm⁻³)	—	—	—	6.8×10^{14} (exp.)
N_D (cm⁻³)	1×10^{20}	2×10^{19}	1×10^5	—[40]

CsPbBr₃ employed as a perovskite with a band gap of 3.6 eV. The suggested device architecture of (FTO/TiO₂/CsPbBr₃/NiOₓ/C) has been depicted schematically in Fig. 10a. Table 3 contains a summary of the simulation parameters as shown in below.

J–V characteristics and quantum efficiency (Q.E) curves have been depicted in Fig. 10b and c, respectively. From the *J–V* measurements we observed the PCE of 13.9% (J_{sc} of 11.07 mA cm⁻², V_{oc} of 1.89 V, FF of 66.6%) for proposed solar cell (SC). Quantum efficiency (Q.E) for simulated solar cell showing a high quantum efficiency at visible region ranging from

390 nm to 530 nm, which is indicated to a considerable optical characteristics of proposed SC.

Literature study indicated that, Ruxin Guo *et al.* reported an efficiency of 11.21% by introducing an ionic liquid (DTPT) into CsPbBr₃-based solar cell (SC) and that is the maximum PCE value ever recorded experimentally for CsPbBr₃-based SC.[41]

In 2018, Haiwen Yuan *et al.* implanted NiOₓ as hole transporting material in CsPbBr₃-based SC and obtained a PCE of 7.29%.[42] Most recently, Yu Zou *et al.* also fabricated a CsPbBr₃-photovoltaic device with incorporating NiOₓ nano-crystal thin
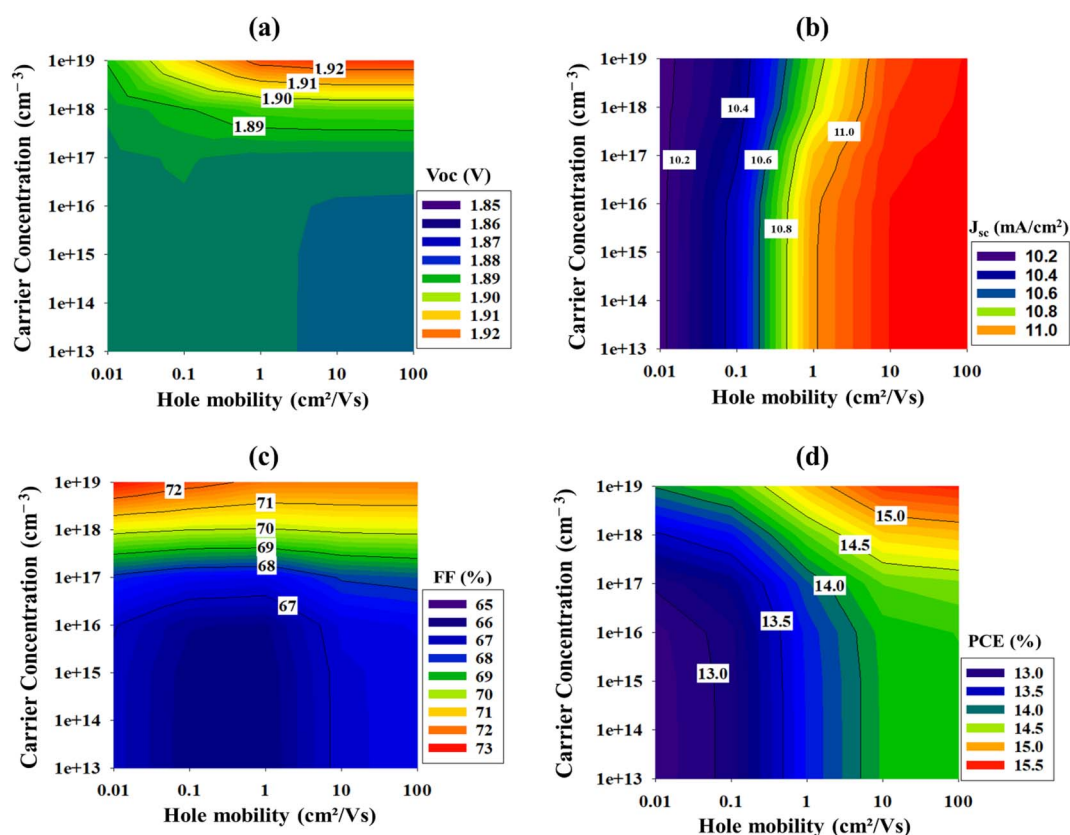

Fig. 11 (a) Performance parameters of CsPbBr₃ solar cell with different carrier concentration (*p*) and hole mobility (μ_p) of NiOₓ HTL layer (a) μ_p *vs. p vs. V_oc* (b) μ_p *vs. p vs. J_sc* (c) μ_p *vs. p vs.* FF (%) (d) μ_p *vs. p vs.* PCE (%).

Table 4 Comparative analysis of electrical properties of deposited NiO_x thin film with the previously published literature

NiO_x thin film	Carrier concentration (cm^{-3})	Hole mobility ($cm^2\ V^{-1}\ s^{-1}$)	References
Boric acid mediated (BA)-NiO_x	2.17×10^{19}	5.35×10^{-2}	46
NiO_x	4.08×10^{18}	2.41×10^{-2}	46
Fe-NiO_x	3.331×10^{12}	6.22	47
NiO_x	1.93×10^{12}	2.60	47
Cu-NiO_x	2.16×10^{16}	40×10^{-2}	48
NiO_x	1.50×10^{16}	14×10^{-2}	48
NiO_x	1.37×10^{17}	1.32×10^{-3}	49
TPA-derived NiO_x	6.8×10^{14}	2	This work

film and enhanced the efficiency at around 9.19%.[43] In order to investigate the potential of NiO_x as a HTL layer in CsPbBr$_3$-based SC, a numerical simulation was carried out to elucidate the combinatorial effects of carrier concentration and hole mobility of NiO_x thin film on the overall photovoltaic performance parameters of CsPbBr$_3$ device.

Fig. 11, illustrates the performance parameters of simulated CsPbBr$_3$ solar cell with different carrier concentration and hole mobility of NiO_x HTL layer. To investigate the influence of HTL carrier concentration (p) and hole mobility (μ_p) on device performances, p and μ_p were varied from 1×10^{13} cm^{-3} to 1×10^{19} cm^{-3} and 0.001 $cm^2\ V^{-1}\ s^{-1}$ to 100 $cm^2\ V^{-1}\ s^{-1}$, respectively. According to Fig. 11, the maximum values of p (1×10^{19} cm^{-3}) and μ_p (100 $cm^2\ V^{-1}\ s^{-1}$) provide the highest PCE value at around 15.44% for simulated device. The reason of the increment in PCE value is due to fact that, when p rises HTL's internal electric field also rises, causing an increase in charge conductivity and transport velocity.[44] On the other hand, an increment in hole mobility (μ_p) will increase the diffusion length of charge carriers, that will make it easier to transport charge carriers without large amount of recombination and subsequently resulting higher PCE value.[45] Table 4 below shows the carrier concentration and hole mobility of NiO_x thin film from the various previous works, as well as the values obtained from this study.

By comparing the results from Fig. 11 and Table 4, it is evident that, there exist a large room for improvement in both carrier concentration and hole mobility parameters of NiO_x thin film that needs to be implemented, if the current record efficiency of CsPbBr$_3$ solar cell is to be surpassed.

4 Conclusions

In this work, MOF derived NiO_x nanoparticles were synthesized by utilizing four distinct ligands (**BTC/TPA/ATPA/DHTPA**). A comparative investigation on the structural, morphological and optical properties of the MOF-derived synthesized NPs have been carried out. The findings of the FeSEM analysis demonstrate that the synthesized NiO_x NPs have variable morphological structure, depending on the ligand of MOFs as well as with the calcination temperature. From the FeSEM, it was observed that, the TPA-derived NiO_x exhibited relatively a small particle size (25–50 nm) with homogenous distribution compare to others, where ATPA derived NiO_x NPs showed the most

significant morphological changes. The fabrication of NiO_x-thin film was also carried out by employing TPA-derived NiO_x (600 °C). The structural, optical and electrical characteristics of the thin film have also been studied, where thin film showing a cubic phase structure with the band gap of 3.25 eV. Carrier concentration, hole mobility and resistivity were measured to be 6.8×10^{14} cm^{-3}; 4.7×10^{14} Ω cm and 2.0 $cm^2\ V^{-1}\ s^{-1}$, respectively. A numerical simulation was also performed to investigate the photovoltaic performance of the TPA-derived NiO_x thin film. The efficiency of the device was measured at around 13.9% with the J_{sc} of 11.07 mA cm^{-2}, V_{oc} of 1.89 V and FF of 66.6%.

Conflicts of interest

There are no conflicts to declare.

Acknowledgements

References

1 Y. Wu, Y. He, T. Wu, T. Chen, W.-z. Weng and H.-L. Wan, *Mater. Lett.*, 2007, **61**, 3174–3178.

2 K. Anandan and V. Rajendran, *Mater. Sci. Semicond. Process.*, 2011, **14**, 43–47.

3 M.-S. Wu and Y.-P. Lin, *Electrochim. Acta*, 2011, **56**, 2068–2073.

4 Y. Wang, J. Zhu, X. Yang, L. Lu and X. Wang, *Thermochim. Acta*, 2005, **437**, 106–109.

5 Y.-Z. Zheng and M.-L. Zhang, *Mater. Lett.*, 2007, **61**, 3967–3969.

6 A. Aslani, V. Oroojpour and M. Fallahi, *Appl. Surf. Sci.*, 2011, **257**, 4056–4061.

7 A. C. Johnston-Peck, J. Wang and J. B. Tracy, *ACS Nano*, 2009, **3**, 1077–1084.

8 J. Bandara, C. M. Divarathne and S. D. Nanayakkara, *Sol. Energy Mater. Sol. Cells*, 2004, **81**, 429–437.

9 R. Kaneko, H. Kanda, K. Sugawa, J. Otsuki, A. Islam and M. K. Nazeeruddin, *Sol. RRL*, 2019, **3**, 1900172.

10 X. Wang, J. Song, L. Gao, J. Jin, H. Zheng and Z. Zhang, *Nanotechnology*, 2005, **16**, 37.

11 P. Justin, S. K. Meher and G. R. Rao, *J. Phys. Chem. C*, 2010, **114**, 5203–5210.

12 Y.-H. Seo, I. H. Cho and S.-I. Na, *J. Alloys Compd.*, 2019, **797**, 1018–1024.

13 P.-H. Lee, T.-T. Wu, C.-F. Li, D. Głowienka, Y.-H. Sun, Y.-T. Lin, H.-W. Yen, C.-G. Huang, Y. Galagan, Y.-C. Huang and W.-F. Su, *Chem. Eng. J.*, 2021, **412**, 128746.

14 S. Wang, Y. Li, J. Yang, T. Wang, B. Yang, Q. Cao, X. Pu, L. Etgar, J. Han, J. Zhao, X. Li and A. Hagfeldt, *Angew. Chem., Int. Ed.*, 2022, **61**, e202116534.

15 S. Pilban Jahromi, N. M. Huang, M. R. Muhamad and H. N. Lim, *Ceram. Int.*, 2013, **39**, 3909–3914.

16 G. Thangamani J., K. Deshmukh, B. Ahamed, K. Chidambaram, K. Saranya and S. Pasha, *Int. J. ChemTech Res.*, 2015, **8**, 974–4290.

17 Y. Sun and H.-C. Zhou, *Sci. Technol. Adv. Mater.*, 2015, **16**, 054202.

18 D. Y. Heo, H. H. Do, S. H. Ahn and S. Y. Kim, *Polymers*, 2020, **12**, 2061.

19 L. Pan, T. Muhammad, L. Ma, Z.-F. Huang, S. Wang, L. Wang, J.-J. Zou and X. Zhang, *Appl. Catal., B*, 2016, **189**, 181–191.

20 T. Prabhakaran, R. V. Mangalaraja, J. C. Denardin and J. A. Jiménez, *J. Alloys Compd.*, 2017, **716**, 171–183.

21 N. C. Horti, M. D. Kamatagi, S. K. Nataraj, M. N. Wari and S. R. Inamdar, *Nano Express*, 2020, **1**, 010022.

22 S. Suresh and J. Podder, *Int. J. Nanopart.*, 2015, **8**, 289–301.

23 Q. Hongxia, W. Zhiqiang, Y. Hua, Z. Lin and Y. Xiaoyan, *J. Nanomater.*, 2009, 479.

24 V. Selvanathan, M. Shahinuzzaman, S. Selvanathan, D. K. Sarkar, N. Algethami, H. I. Alkhammash, F. H. Anuar, Z. Zainuddin, M. Aminuzzaman, H. Abdullah and M. Akhtaruzzaman, *Catalysts*, 2021, **11**, 1523.

25 N. Saikumari, S. M. Dev and S. A. Dev, *Sci. Rep.*, 2021, **11**, 1734.

26 T. Sinha, L. Verma and A. Khare, *Appl. Phys. A: Mater. Sci. Process.*, 2020, **126**, 867.

27 W. W. Lestari, I. D. Winarni and F. Rahmawati, *IOP Conf. Ser.: Mater. Sci. Eng.*, 2017, **172**, 012064.

28 F. Wang, X. Chen, L. Chen, J. Yang and Q. Wang, *Mater. Sci. Eng., C*, 2019, **96**, 41–50.

29 R. Salama, S. Abd El-Hakam, S. Samra, S. El-dafrawy and A. Ahmed, *Int. J. Mod. Chem.*, 2018, **20**(10), 195–207.

30 S. Yang, J. Zhang, C. Bai and K. Deng, *Can. J. Chem.*, 2020, **99**, 465–473.

31 Y. Liao, C. Li, X. Lou, P. Wang, Q. Yang, M. Shen and B. Hu, *J. Colloid Interface Sci.*, 2017, **506**, 365–372.

32 J.-J. Song, B. He, X. Wang, Y. Guo, C. Peng, Y. Wang, Z. Su and Q. Hao, *J. Mater. Sci.*, 2021, **56**, 17178–17190.

33 S. D. Khairnar and V. S. Shrivastava, *J. Taibah Univ. Sci.*, 2019, **13**, 1108–1118.

34 S. Pilban Jahromi, A. Pandikumar, B. T. Goh, Y. S. Lim, W. J. Basirun, H. N. Lim and N. M. Huang, *RSC Adv.*, 2015, **5**, 14010–14019.

35 Z. Sabouri, N. Fereydouni, A. Akbari, H. A. Hosseini, A. Hashemzadeh, M. S. Amiri, R. Kazemi Oskuee and M. Darroudi, *Rare Met.*, 2020, **39**, 1134–1144.

36 A. Barakat, M. Al-Noaimi, M. Suleiman, A. S. Aldwayyan, B. Hammouti, T. B. Hadda, S. F. Haddad, A. Boshaala and I. Warad, *Int. J. Mol. Sci.*, 2013, **14**, 23941–23954.

37 S.-J. Hong, H.-J. Mun, B.-J. Kim and Y.-S. Kim, *Micromachines*, 2021, **12**, 1168.

38 Z.-W. Huang, S.-H. Yang, Z.-Y. Wu and H.-C. Hsu, *ACS Omega*, 2021, **6**, 15855–15866.

39 S. Jana, G. Mondal, B. C. Mitra, P. Bera, B. Chakraborty, A. Mondal and A. Ghosh, *New J. Chem.*, 2017, **41**, 14985–14994.

40 S. Rani, D. Kuar, V. Jeyachandran and D. S. Ghosh, *Opt. Mater.*, 2022, **131**, 112612.

41 R. Guo, J. Xia, H. Gu, X. Chu, Y. Zhao, X. Meng, Z. Wu, J. Li, Y. Duan, Z. Li, Z. Wen, S. Chen, Y. Cai, C. Liang, Y. Shen, G. Xing, W. Zhang and G. Shao, *J. Mater. Chem. A*, 2023, **11**, 408–418.

42 H. Yuan, Y. Zhao, J. Duan, Y. Wang, X. Yang and Q. Tang, *J. Mater. Chem. A*, 2018, **6**, 24324–24329.

43 Y. Zou, F. Cao, P. Chen, R. He, A. Tong, C. Yin, Z. Lan, W. Sun and J. Wu, *Electrochim. Acta*, 2022, **435**, 141392.

44 G. Pindolia, S. M. Shinde and P. K. Jha, *Sol. Energy*, 2022, **236**, 802–821.

45 C. Pinzón, N. Martínez, G. Casas, F. C. Alvira, N. Denon, G. Brusasco, H. Medina Chanduví, A. V. Gil Rebaza and M. A. Cappelletti, *Solar*, 2022, **2**, 559–571.

46 B. Ge, Z. Q. Lin, Z. R. Zhou, H. W. Qiao, A. P. Chen, Y. Hou, S. Yang and H. G. Yang, *Sol. RRL*, 2021, **5**, 2000810.

47 P. S. Chandrasekhar, Y.-H. Seo, Y.-J. Noh and S.-I. Na, *Appl. Surf. Sci.*, 2019, **481**, 588–596.

48 M. Feng, M. Wang, H. Zhou, W. Li, S. Wang, Z. Zang and S. Chen, *ACS Appl. Mater. Interfaces*, 2020, **12**, 50684–50691.

49 X. Jin, Y. Yuan, C. Jiang, H. Ju, G. Jiang, W. Liu, C. Zhu and T. Chen, *Sol. Energy Mater. Sol. Cells*, 2018, **185**, 542–548.